Composition- and Morphology-Dependent Corrosion Stability of Ruthenium Oxide Materials

Svitlana Pylypenko,[†] Berislav B. Blizanac,[‡] Tim S. Olson,[†] Daniel Konopka,[†] and Plamen Atanassov*,[†]

Department of Chemical and Nuclear Engineering, University of New Mexico, 209 Farris Engineering Center, Albuquerque, New Mexico 87131, and Cabot Superior MicroPowders, Albuquerque, New Mexico 87113

ABSTRACT Ruthenium oxide materials were evaluated as possible non-carbon-based supports for fuel cell catalysts. The effects of composition and morphology of ruthenium oxide materials on the conductivity and corrosion stability in the gas-diffusion electrode (GDE) configuration were thoroughly investigated. The compositions of the bulk and surface of three ruthenium oxide materials, along with the surface area and surface morphology, were compared. We have found that all tested ruthenium oxide powders exhibited higher corrosion stability compared to carbon. Full conversion of $RuO_2 \cdot nH_2O$ to the RuO_2 phase by postreduction in a hydrogen atmosphere leads to improved conductivity and corrosion stability.

KEYWORDS: ruthenium oxide • noncarbon • support • corrosion • fuel cell

1. INTRODUCTION

The search for alternative energy is recognized as a very important part of the efforts toward sustainability. Fuel cells are currently explored for automotive, stationary, and portable applications. There has been a substantial acceleration of the research in fuel cell power systems to meet the established targets toward these applications. Improvement of electrocatalytic materials for fuel cells is envisioned mainly through the improvement in their activity and durability and the reduction of catalyst costs.

Carbon blacks are used as supports for the catalytically active phase in state-of-the-art, low-temperature polymer electrolyte membrane (PEM) and phosphoric acid fuel cell (PAFC) electrocatalysts. As such, they are an important component of electrocatalytic layers. Corrosion of the carbon support on the cathode side of a fuel cell has been identified as one of the major detrimental factors in the durability of electrocatalysts and, subsequently, entire fuel-cell-based power devices. The carbon corrosion process is facilitated by the highly corrosive environment of the fuel cells, and also by transient conditions during start-up and shutdown cycles, resulting in cathode voltage excursions to high anodic/oxidative overpotentials. Under such conditions, carbon corrosion is even more pronounced in the presence of a platinum phase, known to catalyze carbon oxidation (1). Earlier studies of carbon corrosion were centered around the PAFCs (2–6). The stability of the carbon supports in PEM

fuel cells is the focus of the latest work in this area (1, 7–9). Increased stability and durability of platinum electrocatalysts supported on carbon is possible through enhancement of the platinum–carbon support interaction by using more corrosion-resistant carbon supports and/or by using platinum alloys (1). Another route to improving the durability of fuel cell systems is to use novel corrosion-resistant noncarbonaceous supports, such as metal oxides.

There are a number of requirements that the new materials have to meet to be considered as catalyst supports in proton-exchange fuel cells. They have to provide good electrical and structural properties at low cost. There have been several reports on the investigations of conductive metal oxides for application as supports (10–15). Sasaki et al. have shown the utilization of metal oxide supports for low-content platinum electrocatalysts (13, 14). They have demonstrated an improved performance of these materials toward oxygen reduction and methanol oxidation. Scheiba et al. have reported the results of their study of hydrous ruthenium oxide as a support for electrocatalysts in DMFCs that showed an increased proton conductivity and catalyst utilization in monoethanolamine (MEA) testing along with limited promotion of carbon monoxide and methanol oxidation (15). The previous investigations of the corrosion stability of hydrous and anhydrous ruthenium oxides were done in the context of their application for the electrolytic evolution of chlorine and oxygen from aqueous solutions (16–18). The anodic corrosion of these materials was linked to the hydrous component, and it was reported that mild heat treatment of the oxide improves the stability and electrocatalytic activity of these materials (16, 18). The majority of the literature reporting the physical characterization of ruthenium oxide materials was done in the context of their application as capacitors (19, 20). The information about the

effect of the structure and morphology on the corrosion stability of ruthenium oxide materials as supports for fuel cell electrocatalysts is very limited. The cost of alternative fuel cell catalyst support materials, such as ruthenium oxide, is a concern. Therefore, increasing the utilization of noncarbonaceous fuel cell catalyst supports should be targeted as a main engineering objective. In the current work, we aim to elucidate potential advantages in the performance characteristics of metal oxide fuel cell catalyst supports.

In this study, we have investigated the corrosion stability of commercially available and produced-in-house ruthenium oxide materials. We have developed a procedure for making gas-diffusion electrodes (GDEs) that contain ruthenium oxide material in the active layer. The performance of ruthenium oxide-based GDEs toward oxygen reduction and the impact of material corrosion on the oxygen reduction performance are evaluated. Conclusions on the effect of the bulk and surface compositions, surface area, and surface morphology on the corrosion stability of the ruthenium oxide materials are discussed.

2. EXPERIMENTAL SECTION

Ruthenium oxide material was produced at Cabot by flame pyrolysis. Another two ruthenium oxide powder materials were obtained from ESPI Metals and J&J Materials. The materials were characterized as received and after postreduction in a hydrogen environment at 250 °C for 2 h. 10 % Pt/Vulcan XC-72 was purchased from ETEK.

Gas-diffusion electrodes (GDEs) were made in a two-step procedure. First, the gas-diffusion layer (GDL) was made by pressing of the 35 wt % Teflon-modified Vulcan XC-72 (XC-35) at 125 °C and 16 000 lb of pressure for 10 min. Next, the ink was prepared as follows: 30 mg of RuO_2, 250 mg of a 5 % Nafion solution, and 650 mg of deionized (DI) water were sonicated for 5 min; then 12 mg of XC-35 and isopropyl alcohol were added and sonicated for another 5 min. The ink was then applied to the GDL layer using a Los Alamos painting technique at 75 °C. Also, electrodes were made using the ink formulation without the carbon, and in this case, the ink was made of RuO_2, Nafion, and DI water only. The GDEs were electrochemically evaluated using a EG&G Princeton Applied Research potentiostat/galvanostat model 273A. Steady-state polarization curves were obtained in galvanostatic mode at room temperature in a 2 M H_2SO_4 liquid electrolyte. For anodic polarization tests, currents ranging from 10 to 30 mA were applied. An acceptable steady-state transient was achieved in 10 min. O_2 was supplied to the air-breathing side of the GDE at atmospheric pressure. For all GDEs, the loading of Ru was 6.7 mg, assuming pure RuO_2. The electrode area was 9.61 cm^2, translating to a RuO_2 loading of 2.1 mg/cm^2. The electrochemically active surface area was calculated by using the specific capacitance for RuO_2 of C = 85 μF/cm^2. In inductively coupled plasma atomic emission spectrometry (ICP-AES) measurements, the acceptable relative standard deviation (RSD) is up to 5.00 %. R^2 of calibration standards is 99.896 %. The minimum acceptable R^2 value is 99.5 %.

X-ray photoelectron spectroscopy (XPS) analysis was performed on a Kratos Axis Ultra X-ray photoelectron spectrometer with a monochromatic Al Kα source operated at 300 W. Data analysis quantification was performed using *CasaXPS* software. The Ru 3d spectrum has two spin–orbit components corresponding to Ru 3d$_{5/2}$ [lower binding energy (BE) side of Ru 3d] and Ru 3d$_{3/2}$ (higher BE side). The separation between these components is 4.2 eV. The data were fitted with a series of mixed Gaussian–Lorentzian functions. The full-width at half-

maximum of the $^3/_2$ components is larger than that of the $^5/_2$ components. The ratio of the primary spin–orbit components and the satellite components was constrained to be 0.67. An asymmetric function was used to curve-fit the RuO_2 component of the Ru 3d peak and the O^{2-} component of the O 1s peak (21). The asymmetric function was used to reflect the fact that the positive hole created by the photoelectric effect interacts with the mobile conduction electrons. C 1s components then were added to complete the curve-fit. X-ray diffraction (XRD) data of samples were acquired with a Bruker D8 Advance powder diffractometer. The angular resolution in 2θ scans was 0.02° for the wide-angle 2θ scans from 20° to 90°. Thermogravimetric analysis (TGA) was performed on a TA Instruments SDT Q600 TGA/DSC. High-resolution transmission electron microscopy (HRTEM) micrographs were obtained on a JEOL 2010 200 kV transmission electron microscope. Scanning electron microscopy (SEM) images were acquired using a Hitachi S-5200 scanning electron microscope.

3. RESULTS AND DISCUSSION

3.1. Physical Characterization.
XRD experiments on powdered RuO_2 materials were carried out to identify the phases present in the materials. The XRD measurements on three different ruthenium oxide parent metal oxides are shown in Figure 1. When compared to the reference (library) data, all three samples are shown to consist of a rutile RuO_2 phase. Significant differences in the diffraction line broadening indicate materials with different crystallite size, translating to differences in the Brunauer–Emmett–Teller (BET) surface area, also indicated in Table 2. The XRD pattern of the reduced Cabot ruthenium oxide material has peaks due to two phases, metallic ruthenium and ruthenium oxide. Quantification of ruthenium oxide versus metallic ruthenium phases, however, is difficult because of the different scattering cross sections for these two phases. Also, it is important to note that XRD is a bulk technique while corrosion processes occur on the surface. A detailed discussion of the surface species is further presented.

Figure 2 shows TGA data collected under a nitrogen atmosphere for the ruthenium oxide materials. There are two distinctive regions of mass loss in the analyzed temperature range, suggesting that there are two types of processes. The weight loss in the temperature range above 1000 °C corresponds to the decomposition of RuO_2 to Ru metal. The weight percent loss measured for all materials in this temperature range is close to the value calculated based on the loss of two oxygen atoms per ruthenium atom. This indicates that ruthenium oxide materials predominantly consist of RuO_2 and do not contain metallic ruthenium. The weight losses observed in the temperature range of 25–500 °C for Cabot and J&J Materials ruthenium oxide materials are most likely due to desorption of bound H_2O and OH groups. On the basis of the weight percent loss in this temperature range, we can speculate that the hydrous content of ruthenium materials is close to 0 % for ESPI Metals material, about 7 % for Cabot material, and about 11 % for J&J Materials ruthenium oxide.

The conductivity of the ruthenium oxide powders was evaluated using a built-in-house device that allowed measurement of the resistance, while controlling the mass and
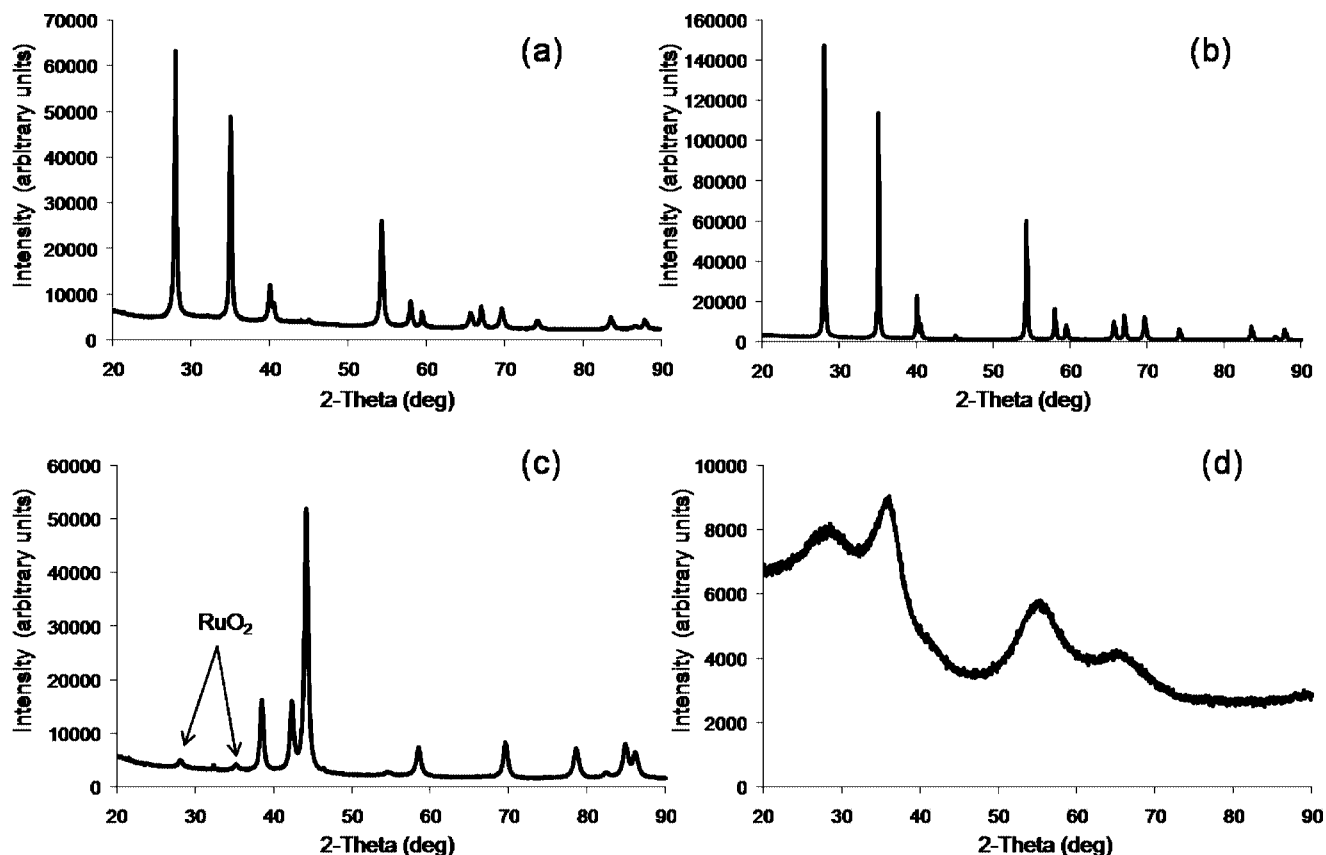
FIGURE 1. XRD patterns of ruthenium oxide materials from (a) Cabot, (b) Cabot, reduced in a hydrogen environment at 250 °C for 2 h, (c) ESPI Metals, and (d) J&J Materials.

Table 1. Curve Fit of High-Resolution Ru 3d XPS Spectra

sample	Ru_1, % RuO_2 screened final state	Ru_2, % $RuO_2 \cdot nH_2O$	Ru_3, % RuO_2 unscreened final state
RuO_2 (ESPI Metals)	66	15	19
RuO_2 (J&J Materials)	54	27	19
RuO_2 (Cabot) + XC-35	24	47	28
reduced RuO_2 (Cabot) + XC-35	88	0	12

Table 2. Results of the Corrosion Stability Measurements of Ruthenium Oxide Materials: Values of Corrosion Current and ICP-AES Analysis

sample	BET, m^2/g	I at 1.2 V RHE, mA	I/mass, mA/mg	I/BET, mA/m^2	I/ESA, mA/m^2	concn, mg/L	RSD of three replicates, %	Ru loss, %
RuO_2 (ESPI Metals)	7	8.4	1262	156.5	30.5	0.179	1.74	0.5
RuO_2 (J&J Materials)	122	24	3605	30.3	11.9	0.184	1.72	0.6
RuO_2 (Cabot) + XC-35	38	5.4	811	25.4	38.1	2.69	0.8	8.1
Reduced RuO_2 (Cabot) + XC-35	17	8	1202	72.1	100.0	1.089	0.47	3.3

thickness of the oxide layer. Considering that the bulk of the material consists of ruthenium in the 4+ oxidation state, all three materials should display significant (metal-like) electronic conductivity. Ruthenium oxide materials (ESPI Metals and J&J Materials) have electric resistivity below the detection limit of the multimeter used, indicating sufficient conductivity of these materials. It may seem surprising that for the Cabot ruthenium oxide the XRD measurements confirm the existence of an electronically conductive phase, but electronic conductivity measurements indicate the significant dielectric nature of the material. The reason lies in fact

that the XRD measurements are bulk property measurements and almost insensitive to the surface composition. TGA, while providing information about the water content, does not allow one to differentiate the surface content from the bulk. Therefore, a surface-sensitive tool, such as XPS, has been employed to investigate the surface composition that may be different from the bulk composition.

High-resolution Ru 3d XPS spectra acquired from ruthenium oxide materials shown in Figure 3 demonstrate that surface ruthenium in all materials is in the mixed state. Six components in the Ru 3d spectrum correspond to ruthenium
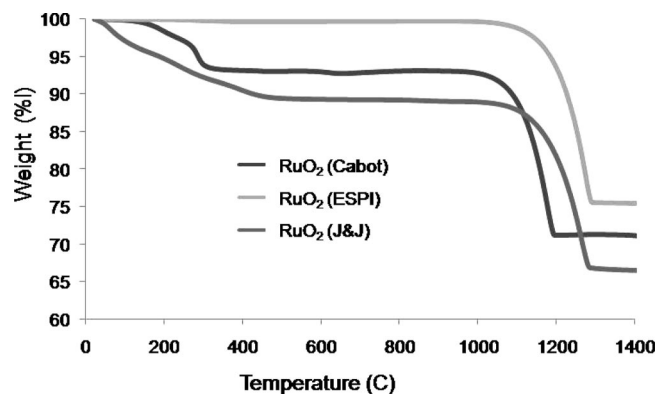
FIGURE 2. TGA analysis of ruthenium oxide materials under nitrogen. Ramp rate 10 °C/min.

components. Components at 280.8 eV ($^5/_2$ component) and 285 eV ($^3/_2$ component) are due to RuO_2. The second doublet is around 282.5 eV ($^5/_2$ component) and 286.7 eV ($^3/_2$ component). A recently published assignment of the peak at 282.5 eV to crystalline ruthenium was based on the visual analysis of the shoulder of the spectrum rather than deconvolution of the spectrum (22). As demonstrated here, deconvolution of the spectrum reveals more than one doublet on as-received ruthenium oxide materials. The changes in the amount of the peak at 282.5 eV are accompanied by the changes in the overall water content determined by TGA and by XPS analysis of oxygen spectra, supporting its assignment to $RuO_2 \cdot nH_2O$. Thus, after reviewing available literature regarding the nature of the species within the BE range of the second component in the ruthenium spectra, we assign

this component to hydrous ruthenium oxide (RuO_xH_y or $RuO_2 \cdot nH_2O$). The third doublet is around 283.5 eV ($^5/_2$ component) and 287.7 eV ($^3/_2$ component). The nature of the peak at 283.5 eV has been the subject of debate in the literature (21). Some believe that this component is due to ruthenium oxide in higher oxidation states, while others attribute this peak to the unscreened final state, shifted to higher BEs as compared to the screened final state at around 281.3 eV. Table 1 shows the relative amounts of species, corresponding to combined $^5/_2$ and $^3/_2$ components of Ru 3d peaks. Among the three materials, ruthenium oxide from ESPI Materials has the highest amount of ruthenium in the RuO_2 form and the lowest amount (15%) in the form of $RuO_2 \cdot nH_2O$. Ruthenium oxide (J&J Materials) has a somewhat higher content of $RuO_2 \cdot nH_2O$ (27%). The main form of ruthenium in Cabot material is $RuO_2 \cdot nH_2O$ (47%). Five components were used to curve-fit O 1s spectra (not shown). The component at 529.4 eV is due to O^{2-} species (oxygen bound to ruthenium). The component at 530.6 eV can be due to RuO_3 and/or OH^-. The peak at 531.6 eV is attributed to OH^- species. The last two components, at 532.8−534 eV, can be assigned to adsorbed H_2O and/or CO and CO_2 species (21). OH^- and H_2O are dominating the structure of the untreated ruthenium oxide (Cabot) material. Generally, water can be bound to the RuO_2 surface as a chemically bound layer and/or physically adsorbed within the micropores (22). The physically adsorbed water is expected to evaporate under UHV conditions and, therefore, is not detected in the O 1s XPS signal.
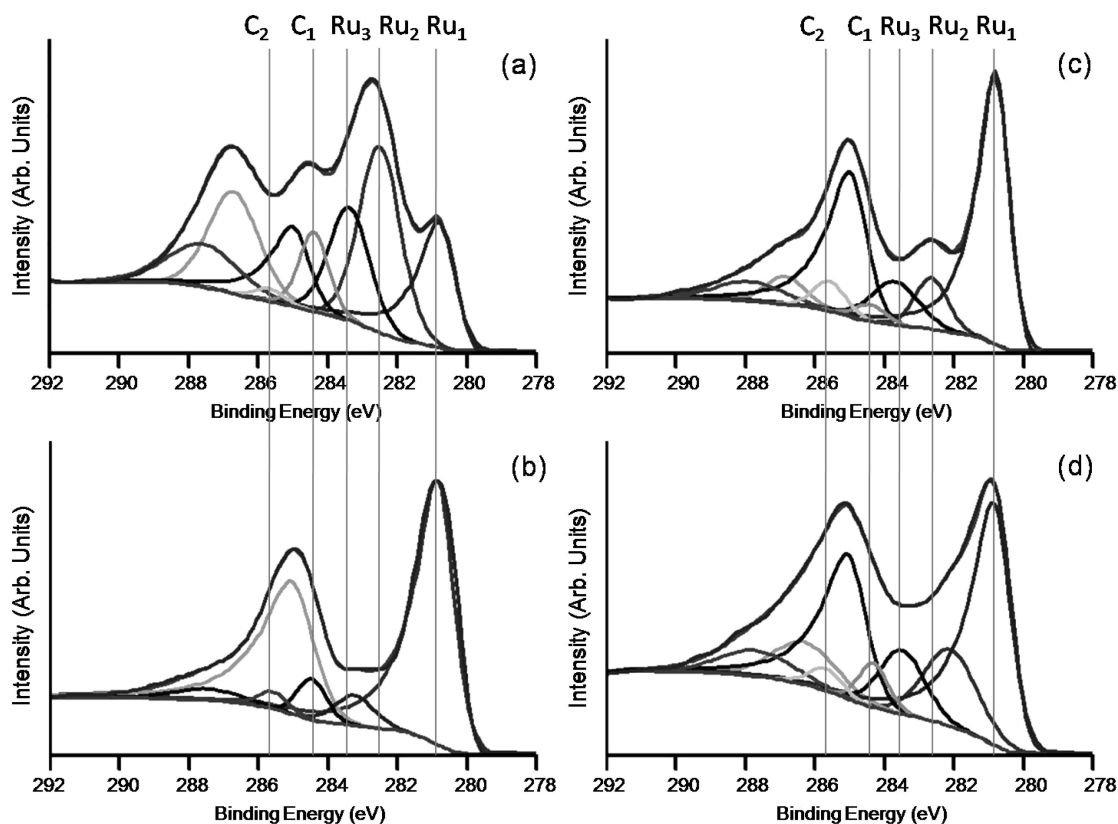

FIGURE 3. High-resolution Ru 3d XPS spectra of ruthenium oxide materials from (a) Cabot, (b) Cabot, reduced in a hydrogen environment at 250 °C for 2 h, (c) ESPI Metals, and (d) J&J Materials.
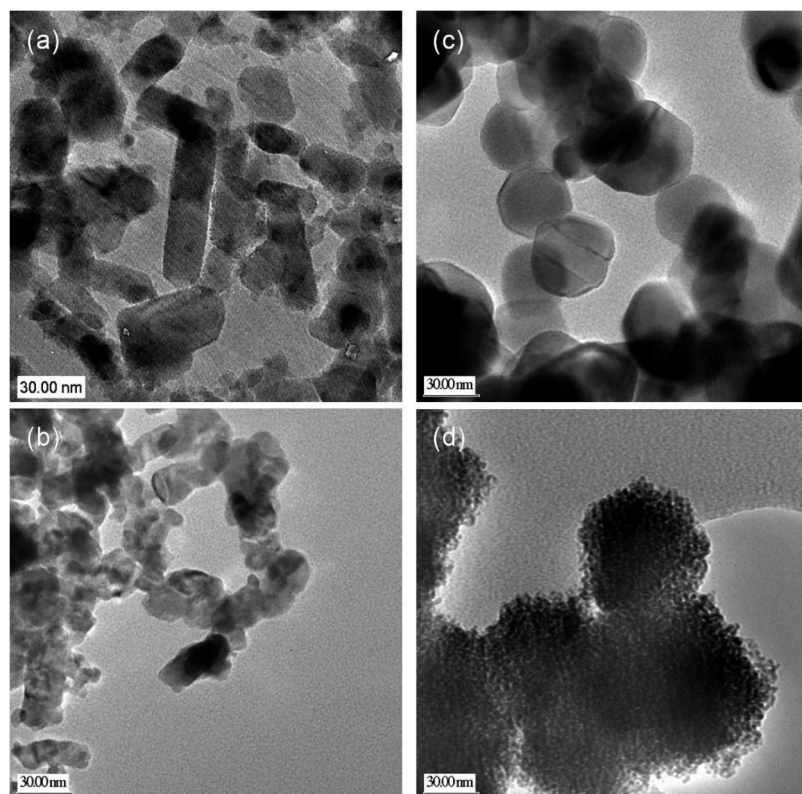
FIGURE 4. HRTEM images of ruthenium oxide materials from (a) Cabot, (b) Cabot, reduced in a hydrogen environment at 250 °C for 2 h, (c) ESPI Metals, and (d) J&J Materials.

Postreduction in a hydrogen atmosphere was used to convert ruthenium to valence IV. After reduction in a hydrogen atmosphere at 250 °C, the amount of RuO_2 significantly increases (Figure 3b). After reduction at 250 °C, concentrations of peaks due to RuO_2 in screened and unscreened final states are are 88 % and 12 %, respectively. $RuO_2 \cdot nH_2O$ was effectively converted to RuO_2. Analysis of O 1s spectra has revealed a significant increase in O^{2-} species and a decrease in OH^- and H_2O. Therefore, the important conclusion is that materials produced on the flame pyrolysis platform with aqueous precursor solutions show bulk conversion to the conductive phase of RuO_2, but the surface composition corresponds to an insulating hydrated state, $RuO_2 \cdot nH_2O$. The increased electronic conductivity of materials exposed to a reducing atmosphere is due to bulk conversion to metallic ruthenium (XRD) and surface conversion to RuO_2 (XPS).

The BET surface area of the Cabot ruthenium oxide was measured to be 38 m^2/g. However, the BET surface area of the reduced material is 17 m^2/g, which is about 2 times lower than the BET of the pristine ruthenium oxide (Cabot). One of the possible explanations of the decrease in the BET surface area can be adherance of the particles to each other. The BET surface area of the ruthenium oxide (ESPI Metals) is 7 m^2/g, which is about 5 times less than the BET surface area of Cabot ruthenium oxide. The ruthenium oxide material obtained from J&J Materials has a much higher surface area than other materials tested in this work. The measured BET surface area is 122 m^2/g.

TEM micrographs of ruthenium oxide powders are presented in Figure 4. TEM micrographs demonstrate various morphologies and particle sizes of these materials. Ruthenium oxide (Cabot) powder consists of particles of elongated shape with lengths in the range of 20−120 nm. The elongated shape of the particles is also observed in a high-magnification SEM image (not shown). TEM micrographs of the ruthenium oxide from Cabot, reduced at 250 °C in a hydrogen atmosphere, indicate that upon reduction the asymmetric shape of the crystallites becomes less pronounced and the size of the particles decreases significantly, although the particles fuse together to form more complex aggregate structures. The morphology of the ruthenium oxide (ESPI Metals) material is drastically different from the morphology of the Cabot material. Contrary to the elongated shape of the particles in the Cabot material (Figure 4a), the ESPI Metals material is relatively monodispersed, hexagonally shaped particles with a diameter of about 50 nm (Figure 4c). The TEM micrograph (Figure 4d) and high-magnification SEM image (not shown) of the ruthenium oxide (J&J Materials) demonstrate that the surface roughness in this material is much higher than that for other RuO_2 materials, leading to a significantly higher BET surface area. Figure 5, representing low-magnification SEM images of ruthenium oxide materials, shows that smaller ruthenium oxide particles form large agglomerates.

3.2. Electrochemical Characterization.
Currently, there are no procedures developed for testing the corrosion stability of noncarbon supports. Subsequently,
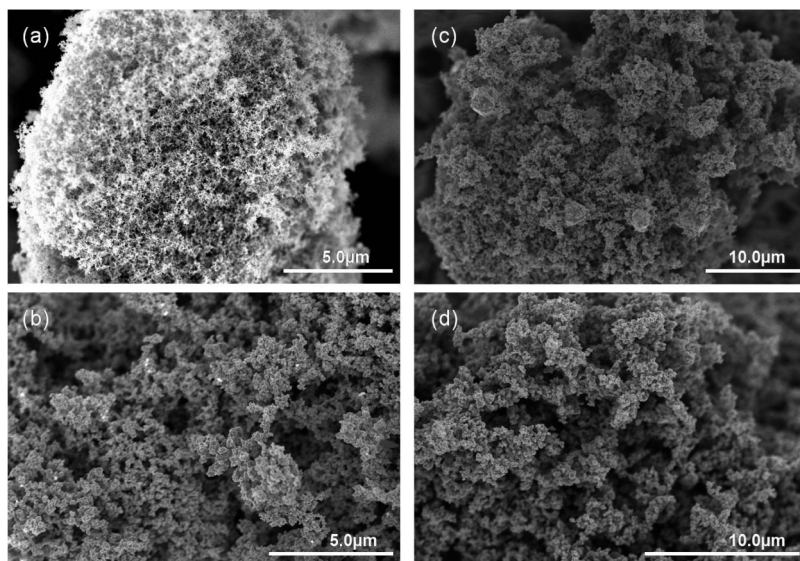
FIGURE 5. SEM images of ruthenium oxide materials from (a) Cabot, (b) Cabot, reduced in a hydrogen environment at 250 °C for 2 h, (c) ESPI Metals, and (d) J&J Materials.
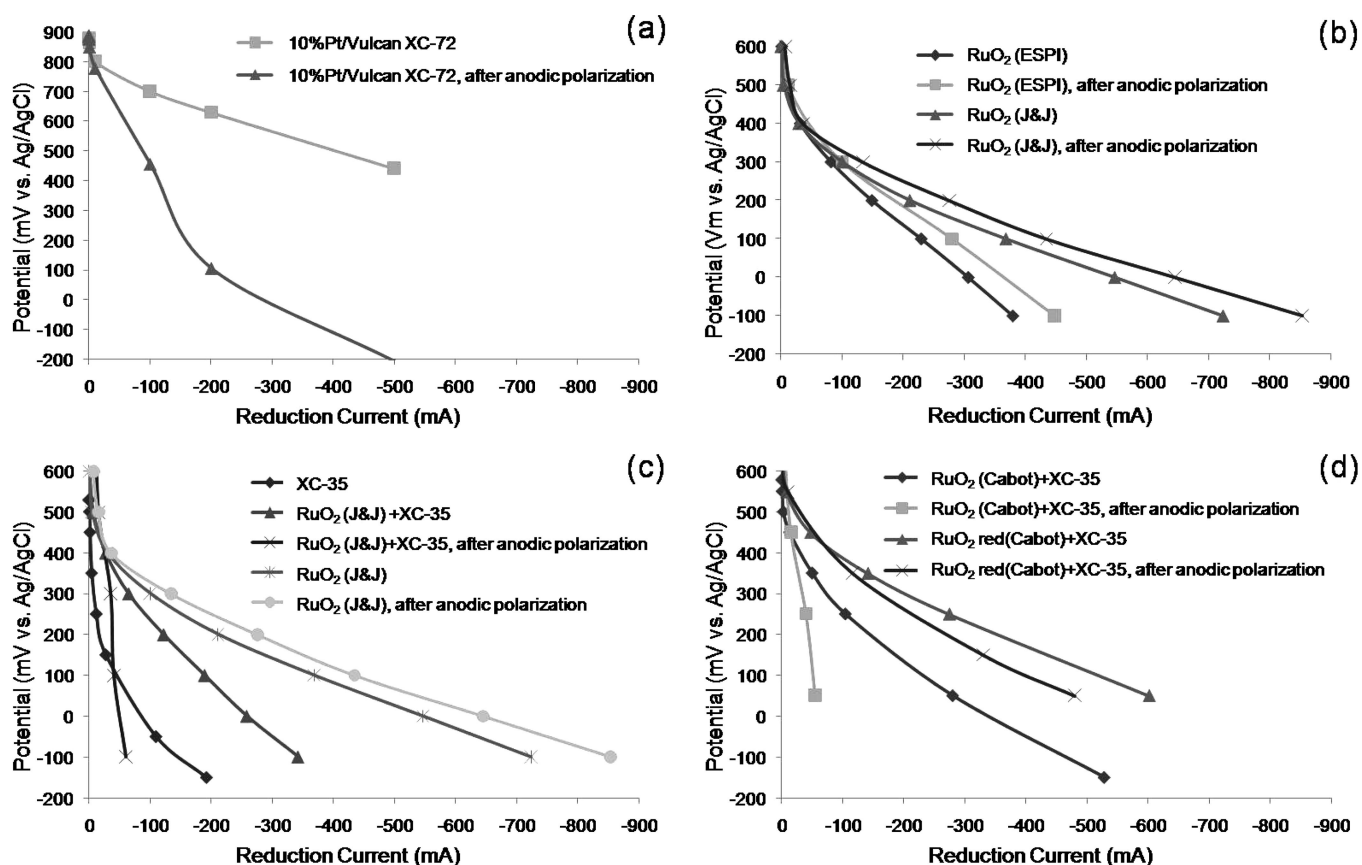

FIGURE 6. Corrosion testing in a gas-diffusion cell in a liquid electrolyte, O_2, 0 psi. Cathodic polarization curves for (a) 10% Pt/Vulcan XC-72 (ETEK), (b) ruthenium oxide materials from ESPI Metals and J&J Materials, (c) ruthenium oxide material from J&J Materials, demonstrating the effect of Teflon-modified carbon, and (d) ruthenium oxide from Cabot, demonstrating the effect of postreduction in hydrogen.

there are no metrics that would indicate what the corrosion stability requirement is, i.e., what is "good enough". In this work, the methodology borrowed from carbon corrosion testing was modified and applied to noncarbon materials. The results of corrosion evaluation are shown in Figure 6. Two cathodic polarization curves for each tested material are shown. The first curve demonstrates the initial performance.

The second curve is obtained after the anodic polarization of the GDE. This anodic polarization was performed to accelerate the corrosion processes that occur during fuel cell operation. The losses in the oxygen reduction performance are result of corrosion of the electrode material. To be able to quantify the material loss during corrosion measurements, after the full corrosion protocol was applied, the

liquid solution was filtered and submitted for ICP analysis. Filtration was necessary to prevent inclusion of the material lost during the physical deterioration of the electrode and to account for only the part resulting from RuO_2 corrosion—dissolution. The results of the corrosion measurements, along with the ICP data, are shown in Table 2.

The oxygen reduction performances before and after anodic polarization of 10% Pt/Vulcan XC-72 (ETEK) and ruthenium oxide (J&J Materials and ESPI Metals) materials are shown in Figure 6a,b. 10% Pt/Vulcan XC-72 tested under the same conditions has shown higher reduction currents compared to ruthenium oxide materials; however, it exhibited lower reduction currents than RuO_2 samples after anodic polarization. The higher overall cathodic (Figure 6b) and anodic (Table 2) currents obtained on ruthenium oxide supplied by J&J Materials compared to the sample provided by ESPI Metals are not due to the intrinsic corrosion stability but are due to the higher BET surface area of the J&J Materials sample. When the anodic current, measured at 1.2 V versus reversible hydrogen electrode scale (RHE), is normalized to the BET surface area and electrochemically accessible surface area (ESA), currents due to corrosion of these two materials are close. Moreover, both of these materials demonstrated no decrease in the oxygen reduction performance associated with corrosion of RuO_2. Slightly higher currents observed after anodic polarization are probably associated with changes in the ESA and/or more complete surface conversion of hydrated $RuO_2 \cdot nH_2O$ to RuO_2. ICP-AES analysis confirmed that the loss of ruthenium due to corrosion is less than 1%. Thus, the corrosion test has shown that ruthenium oxide materials exhibit high corrosion stability. We expect a significant improvement in the oxygen reduction performance of ruthenium oxide upon platinum deposition as well as the preserved corrosion stability of the ruthenium oxide support. Figure 6c demonstrates the differences in the performance of the electrodes made of ruthenium oxide (J&J Materials) with and without the addition of a carbon component (XC-35, Teflon-modified XC-72) in the ink. Significantly lower cathodic currents are observed for the electrode made of ruthenium oxide mixed with Teflon-modified carbon. Reduction of the cathodic current is, however, not due to the RuO_2 dissolution (corrosion) but the physical loss in the ruthenium oxide powder as a result of corrosion of the teflonized carbon matrix within the GDE. This became apparent after the visual inspection of the working solution, where ruthenium oxide precipitate was observed. After the carbon materials were completely excluded from the GDE preparation, the loss of RuO_2 due to the corrosion was much smaller. Figure 6d displays the cathodic polarization curves for Cabot ruthenium oxide. These electrodes were made using a mixture of ruthenium oxide and Teflon-modified carbon, resulting in lower oxygen reduction currents and deterioration of the electrode. However, when the as-received ruthenium oxide (Cabot) and postreduced ruthenium oxide (Cabot) are compared, several observations can be made. The sample made in-house in which incomplete surface conversion to RuO_2, i.e., surface

in the hydrated state, was confirmed by XPS measurements showed initially a high corrosion loss, ca. 8%. A postreduction step in hydrogen at 250 °C after 2 h resulted in a significant improvement in the corrosion stability, as evidenced by cathodic polarization curves and ICP-AES analysis.

4. CONCLUSION

Ruthenium oxide materials with a higher surface concentration of RuO_2 showed superior corrosion stability. The loss of ruthenium during the corrosion tests was less than 1% for these samples. We have found that conversion of hydroxo groups present at the surface of ruthenium oxide materials to the RuO_2 phase by postreduction in a hydrogen atmosphere leads to improved conductivity and corrosion stability. The tested ruthenium oxide materials exhibited higher corrosion stability compared to carbon used to form GDE. When carbon-containing GDEs were subjected to corrosion measurements, false characterization originated from corrosion of the carbon powder in the electrode and a loss in the interfacial contact between the teflonized carbon and metal oxide. At this stage, it has been assumed that a loss of less than 5% ruthenium, after the full corrosion stability protocol, is sufficient for DMFC cathode applications. This assumption, as well as the performance of platinum supported on ruthenium oxide, will have to be verified in MEA measurements, by evaluating the effect of corrosion on the MEA and membrane performance.

REFERENCES AND NOTES

(1) Yu, X. W.; Ye, S. Y. *J. Power Sources* **2007**, *172*, 145–154.
(2) Giordano, N.; Antonucci, P. L.; Passalacqua, E.; Pino, L.; Arico, A. S.; Kinoshita, K. *Electrochim. Acta* **1991**, *36*, 1931–1935.
(3) Gruver, G. A. *J. Electrochem. Soc.* **1978**, *125*, 1719–1720.
(4) Kinoshita, K. *Carbon—Electrochemical and Physicochemical Properties*; John Wiley & Sons, Inc.: New York, 1988.
(5) Kinoshita, K.; Bett, J. *Carbon* **1973**, *11*, 237–247.
(6) Antonucci, P. L.; Romeo, F.; Minutoli, M.; Alderucci, E.; Giordano, N. *Carbon* **1988**, *26*, 197–203.
(7) Arico, A. S.; Stassi, A.; Modica, E.; Ornelas, R.; Gatto, I.; Passalacqua, E.; Antonucci, V. *J. Power Sources* **2008**, *178*, 525–536.
(8) Dowlapalli, M. R.; Atanassov, P.; Xie, J.; Rice, G. *ECS Trans.* **2006**, *1*, 41.
(9) Maass, S.; Finsterwalder, F.; Frank, G.; Hartmann, R.; Merten, C. *J. Power Sources* **2008**, *176*, 444–451.
(10) Chen, G. Y.; Bare, S. R.; Mallouk, T. E. *J. Electrochem. Soc.* **2002**, *149*, A1092–A1099.
(11) Garcia, B. L.; Fuentes, R.; Weidner, J. W. *Electrochem. Solid State Lett.* **2007**, *10*, B108–B110.
(12) Ioroi, T.; Senoh, H.; Yamazaki, S. I.; Siroma, Z.; Fujiwara, N.; Yasuda, K. *J. Electrochem. Soc.* **2008**, *155*, B321–B326.
(13) Sasaki, K.; Adzic, R. R. *J. Electrochem. Soc.* **2008**, *155*, B180–B186.
(14) Sasaki, K.; Zhang, L.; Adzic, R. R. *Phys. Chem. Chem. Phys.* **2008**, *10*, 159–167.

(15) Scheiba, F.; Scholz, M.; Cao, L.; Schafranek, R.; Roth, C.; Cremers, C.; Qiu, X.; Stimming, U.; Fuess, H. *Fuel Cells* **2006**, *6*, 439–446.

(16) McMurra, H. N. *J. Mater. Chem.* **1994**, *4*, 1283–1287.

(17) Mill, A.; Gidding, S.; Pate, I. *J. Chem. Soc., Faraday Trans. 1* **1987**, *83*, 2317–2329.

(18) Mill, A.; Lawrenc, C.; Eno, R. *J. Chem. Soc., Chem. Commun.* **1984**, *1984*, 1436–1438.

(19) Fang, W. C.; Huang, J. H.; Chen, L. C.; Su, Y. L. O.; Chen, K. H. *J. Power Sources* **2006**, *160*, 1506–1510.

(20) Sugimoto, W.; Yokoshima, K.; Murakami, Y.; Takasu, Y. *Electrochim. Acta* **2006**, *52*, 1742–1748.

(21) Rochefort, D.; Dabo, P.; Guay, D.; Sherwood, P. M. A. *Electrochim. Acta* **2003**, *48*, 4245–4252.

(22) Foelske, A.; Barbieri, O.; Hahn, M.; Kotz, R. *Electrochem. Solid State Lett.* **2006**, *9*, A268–A272.

AM800170K